Physics with isotopically controlled semiconductors

© E.E. Haller¶

Department of Materials Science and Engineering, University of California at Berkeley and Materials Sciences Division,
Lawrence Berkeley National Laboratory,
Berkeley, CA 94720 USA

(Получена 26 ноября 2009 г. Принята к печати 1 декабря 2009 г.)

This paper is based on a tutorial presentation at the International Conference on Defects in Semiconductors (ICDS-25) held in Saint Petersburg, Russia in July 2009. The tutorial focused on a review of recent research involving isotopically controlled semiconductors. Studies with isotopically enriched semiconductor structures experienced a dramatic expansion at the end of the Cold War when significant quantities of enriched isotopes of elements forming semiconductors became available for worldwide collaborations. Isotopes of an element differ in nuclear mass, may have different nuclear spins and undergo different nuclear reactions. Among the latter, the capture of thermal neutrons which can lead to neutron transmutation doping, is the most prominent effect for semiconductors. Experimental and theoretical research exploiting the differences in all the properties has been conducted and will be illustrated with selected examples.

1. Introduction

Isotopes of a given element have identical numbers of protons but differ in the number of neutrons making up their nuclei. In crystalline solids, this difference in nuclear mass most directly affects vibrational phenomena, i. e., phonon frequencies and all phonon-related properties. These include lattice constant, thermal conductivity, electronic band gaps, localized vibrational modes and self-diffusion, to name a few. Further differences between isotopes of an element are found in their nuclear spins and in the cross sections for nuclear reactions, most importantly the capture of thermal neutrons.

The existance of isotopes became established over a period of time by Soddy [1], Thomson [2] and Aston [3]. Until the massive efforts during World War II which led to separation and enrichment of isotopes in the tens of kilograms, isotope separation led to minute quantities of materials, too small and too expensive to be practical for solid state studies. After WWII, the first isotopically enriched semiconductor single crystal of ^{74}Ge was grown at Bell Laboratories for thermal conductivity studies [4]. The starting material came from Oak Ridge National Laboratory. At prices ranging from a few to a few tens of US dollars per milligram, any sizable quantities of enriched semiconductor isotopes remained out of reach for the typical solid state researcher.

The high costs of isotope-related semiconductor studies were no longer a limiting factor after the end of the Cold War. For some years, Russian and Ukrainian isotope enrichment plants had converted a fraction of their weapons-related isotope production to the enrichment of a wide range of elements. The resulting large reserves of isotopes of a wide variety of semiconductor-forming elements, including but not limited to C (diamond), Si, Ge and Ga, became accessible for research collaborations. This conversion from the use of isotopes for weapons to civilian applications is a classic case of „swords to plowshares“ as aptly described by Cardona [5].

¶ E-mail: eehaller@lbl.gov

2. Thermal conductivity

From an applications point of view, the most important phonon-related effect is the thermal conductivity of a crystalline solid. The removal of the heat produced by a modern semiconductor integrated circuit running at a clock frequency of several GHz has become an obstacle for further improvements of device performance. It is no surprise that one of the expectations for isotopically enriched semiconductors has been increases in thermal conductivity. From a number of careful recent studies of the thermal conductivity in diamond, silicon and germanium, we conclude that near and above room temperature increases in the range of at most tens of percent can be expected.

The thermal conductivity of dielectrics is given by

$$K = \frac{1}{3} C v L, \tag{1}$$

with C — specific heat, v — phonon velocity and L — phonon mean-free path [6]. Neither the velocity of low-frequency phonons nor the specific heat which has been determined by Morelli et al. [7] are predicted to change much at a 1% isotope impurity level. The large thermal conductivity increases which are observed for diamonds with increasing isotopic purity must be due to changes in the phonon scattering rates. This suggestion goes back to Pomeranchuk [8].

Wei et al. [9] have measured a record thermal conductivity of 410 W/(cm · K) at 104 K for a 99.9% ^{12}C enriched diamond (Fig. 1). They fitted their data with the Callaway model [10] using four independent scattering processes. The functional form of the individual scattering rates were chosen as follows:

$$\frac{1}{\tau_{\text{norm}}} = \frac{A v T^3}{\lambda}, \tag{2}$$

$$\frac{1}{\tau_{\text{umklapp}}} = \frac{B v T}{\lambda} \exp\left(-\frac{C}{T}\right), \tag{3}$$

$$\frac{1}{\tau_{\text{bound}}} = \frac{v}{D}, \tag{4}$$

$$\frac{1}{\tau_{\text{isotope}}} = \frac{4\pi^3 v V_0 x(1-x)}{\lambda^4 (12+x)^2}, \tag{5}$$

with v and λ corresponding to the average phonon velocity and wavelength, respectively; x is the isotope fraction of ^{13}C, V_0 is the atomic volume and T is the absolute temperature. The constants A, B, C and D were determined from the fits:

$$A = 7.2 \cdot 10^{-11}\,\text{cm/K}^3, \quad B = 1.5 \cdot 10^{-12}\,\text{cm/K},$$

$$C = 670\,\text{K} \quad \text{and} \quad D = 0.33\,\text{cm}.$$

Once the constants A through D have been determined it is possible to predict the dependence of thermal conductivity on temperature and isotopic composition. This has led to their prediction of a thermal conductivity as great as $2000\,\text{W}/(\text{cm} \cdot \text{K})$ near 80 K, exceeding Geballe's prediction [11] that the thermal conductivity of pure diamond may surpass $1000\,\text{W}/(\text{cm} \cdot \text{K})$ around liquid nitrogen temperature (77 K). Similar results have been reported by Olson et al. [12]. It should be pointed out that measurements of such extreme thermal conductivities for millimeter-size samples are extremely difficult. The samples act like close to perfect thermal short circuits.

Thermal conductivity studies have also been performed on very highly enriched, ultrapure ^{70}Ge crystals (Fig. 2) [13]. In these 99.99% enriched single crystals, the thermal conductivity exceeds the maximum values recorded by Geballe and Hull [4] by a factor of ~ 3. Further detailed measurements have been conducted and an in-depth analysis has been reported [14].

The thermal conductivities of both a Si single crystal of natural composition and an isotopically enriched one have been measured over a wide temperature range by T. Ruf et al. Their original results showed a 60% increase of the room temperature thermal conductivity of highly enriched ^{28}Si over $^{\text{nat}}$Si [15]. Later they revised their original high temperature values of the thermal conductivity of the enriched ^{28}Si from 60% to $10 \pm 2\%$ over the values of the $^{\text{nat}}$Si crystal. This significantly lower value is in line with experimental observations of other groups and with theoretical estimates [16].

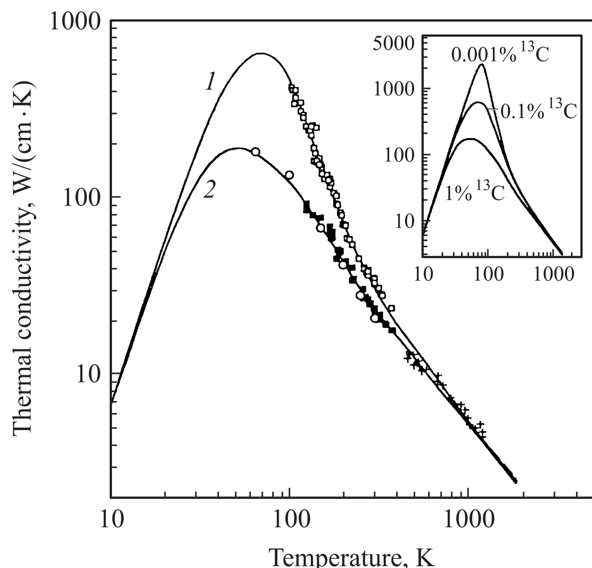

Fig. 1. Thermal conductivity of diamond with natural abundance (1.1% ^{13}C) (curve *2*), and isotopically enriched (0.1% ^{13}C) diamond (curve *1*). The inset shows the calculated thermal conductivity corresponding to 1%, 0.1%, and 0.001% ^{13}C concentrations according to the Callaway theory [10] (Adapted from Wei et al. [9]).

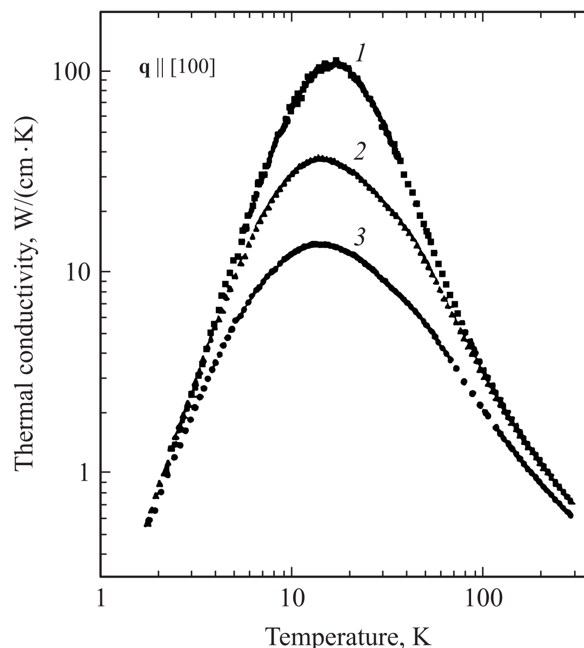

Fig. 2. Temperature dependence of the thermal conductivity along the [100] direction of germanium single crystals with different isotopic composition, % ^{70}Ge: *1* — 99.99, *2* — 96.3, *3* — natural Ge [13].

3. Phonons

3.1. Bulk crystals

The simplest dependence of the phonon frequency ω on mass M can be described within the virtual-crystal approximation (VCA) [17,18] by a „spring and ball" model and is given by

$$\omega \propto \frac{1}{M^{1/2}}. \tag{6}$$

The phonon dispersion relationship describes the phonon frequencies ω as a function of the wave vector $\mathbf{k}$ for the various vibrational modes. Raman spectroscopy is ideally suited for the study of optical phonons at $\mathbf{k} = 0$. Photoluminescence in direct band gap semiconductors requires the assistance of $\mathbf{k} \neq 0$ phonons. In germanium, the recombination of an electron at the conduction band minimum

$$\mathbf{k} = \left(\frac{2\pi}{a}\right)\left(\frac{1}{2}, \frac{1}{2}, \frac{1}{2}\right),$$

i.e., L-point with a hole at the valence band maximum $\mathbf{k} = 0$ requires the emission or absorption of a zone

boundary phonon at the L-point to satisfy the conservation of wave vector momentum. Raman spectroscopy and photoluminescence (PL) have been used for the study of phonons in isotopically enriched germanium crystals as well as those with controlled isotopic mixtures.

Fig. 3 shows superimposed Raman lines of natural and of isotopically enriched Ge single crystals recorded near liquid nitrogen temperatures (90 K) [19]. The lines in these spectra are fully resolved instrumentally and their width is caused by homogeneous broadening. The centroid of the Raman line shifts following equation (6). What is surprising at first sight is the very weak dependence of the phonon linewidth of $\sim 1\,\mathrm{cm}^{-1}$ on isotopic composition. The close to constant linewidth has been explained with phonon delocalization [20–24] which can be discussed within the framework of Anderson localization [25]. If we express the relative mass fluctuations $\Delta M/\overline{M}$ in the form of a frequency bandwidth $(\Delta M/\overline{M})\ \omega_0 = 12\,\mathrm{cm}^{-1}$ with ω_0 being the angular optical phonon frequency at $\mathbf{k} = 0$ and compare it with the bandwidth of the optical phonons in the first Brillouin zone $\Delta\omega_0 \approx 100\,\mathrm{cm}^{-1}$, we immediately see that the mass fluctuation bandwidth is much smaller than the intrinsic optical phonon bandwidth. Under the circumstances phonons do not become localized on individual atoms but remain spread out over a large number of unit cells, leading to a close to perfect linear averaging of the various isotope masses.

The Raman linewidth has been shown to be due to the phonon lifetime (τ) for the anharmonic decay into two phonons. In good approximation one writes:

$$\Delta\omega_0\tau \approx 1. \qquad (7)$$

Time-resolved measurements have yielded lifetimes of 6 ps in very good agreement with the observed $\Delta\omega_0 = 1\,\mathrm{cm}^{-1}$ (equivalent to $3\cdot10^{10}$ Hz) [20]. This natural linewidth

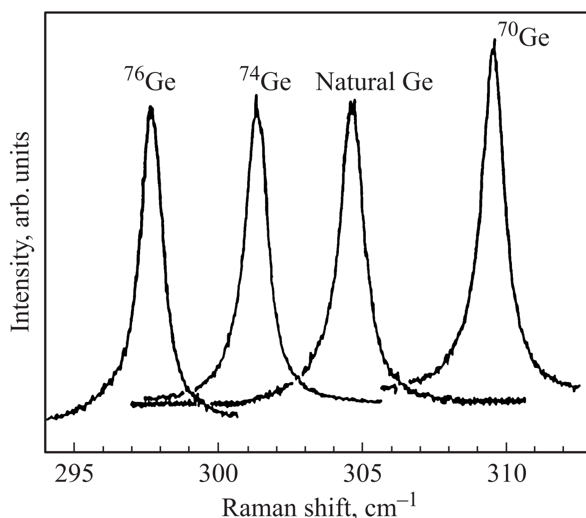

Fig. 3. Raman spectra of the optical zone center phonon of several isotopically enriched Ge crystals and of a natural Ge crystal at 90 K (Courtesy of Fuchs et al. [19]).

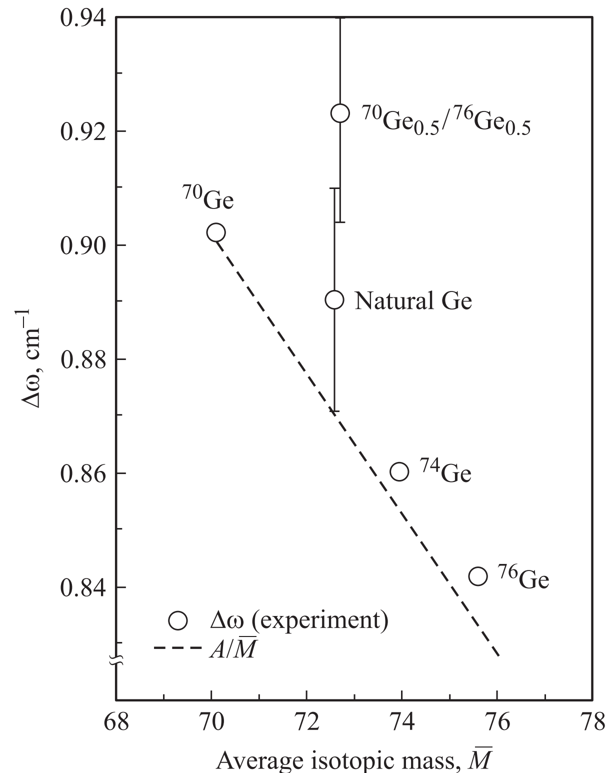

Fig. 4. Full width at half maximum of the Raman lines shown in Fig. 3 and of a $^{70}Ge_{0.5}/^{76}Ge_{0.5}$ sample. The dashed line represents the M^{-1} dependence for isotopically pure samples (Courtesy of Fuchs et al. [19]).

(or lifetime) is dominated by anharmonic interactions leading to the decay of an optical phonon at $\mathbf{k} = 0$ into two phonons. At the low temperature where these Raman experiments were conducted, the rate for anharmonic decay (τ^{-1}) is proportional to the amplitudes of the two phonons created in the process:

$$\frac{1}{\tau} = \Delta\omega_0 \propto \langle u_1^2\rangle\langle u_2^2\rangle = \frac{\hbar^2}{4M^2\omega_1\omega_2}. \qquad (8)$$

Using equation (6) $\omega \propto M^{-1/2}$, we find:

$$\delta\omega_0 \propto M^{-1}. \qquad (9)$$

The widths of the Raman lines obtained from the four isotopically enriched Ge crystals indeed follow such a simple dependence (Fig. 4). The Raman linewidths for the crystals of natural composition and of maximum isotope disorder are slightly larger. Cardona et al. [24] have shown that this extra broadening requires the effect of anharmonicity on the density of phonon states for three-dimensional crystals. They further showed that when going to two dimensions, isotope disorder broadening can be explained in the harmonic approximation.

The first photoluminescence studies of several isotopically enriched Ge crystals at low temperatures were reported by Davies et al. [26,27] and by Etchegoin et al. [22].

Fig. 5 shows representative luminescence spectra of highly enriched ^{70}Ge and ^{74}Ge crystals. The longitudinal acoustic (LA) and the transverse optical (TO) phonon assisted free exciton (FE) lines are clearly shifted in energy. Excitons bound to deliberately introduced substitutional Cu acceptors generate both phonon assisted (TA, LA, TO) as well as no-phonon lines (NP). In addition, one observes a sharp no-phonon line due to P donors. Whereas the phonon assisted lines suffer energy shifts due to phonon *and* band gap energy changes, the NP lines are displaced solely because of band gap energy changes. This information allows the quantitative determination of isotope-related phonon and band gap energy changes. After correcting for the band gap shifts, the phonon energies accurately follow the frequency dependence given in Eq. (6).

Stimulated in part by speculations regarding very large increases of the thermal conductivity in isotopically pure diamonds, a series of diamond crystal growth and characterization studies with extensive theoretical interpretation has been conducted. Using the well-established multiple-scattering formalism of the coherent potential approximation (CPA), Hass et al. [28,29] and Chrenko [30] were able to explain quantitatively the large effects of isotopic disorder on the frequencies of optical phonons at $\mathbf{k} = 0$ and for the Raman linewidths for a range of isotopic compositions. Fig. 6 shows the Raman frequencies and linewidths as a function of the fractional ^{13}C concentration. Isotopic disorder causes the upwards bowing of the Raman frequency dependence as well as the large asymmetric increase in linewidth with isotopic composition. Both dependences are well described with CPA theory, especially when the intrinsic linewidth of the isotopically purest samples is subtracted from all the data points.

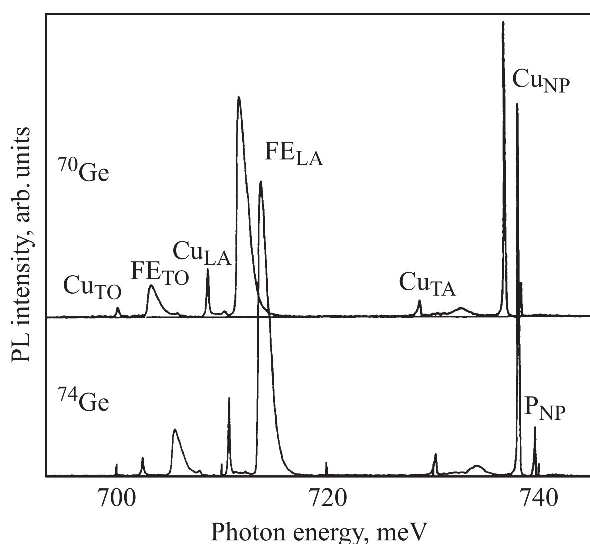

Fig. 5. Luminescence from the decay of free excitons and excitons bound to Cu acceptors and P donors in ^{70}Ge and ^{74}Ge at 4.2 K. The subscripts indicate the *L*-point phonons assisting in the exciton decay. The impurity bound excitons can decay without emission of a phonon (NP) (Courtesy of Davies et al. [26]).

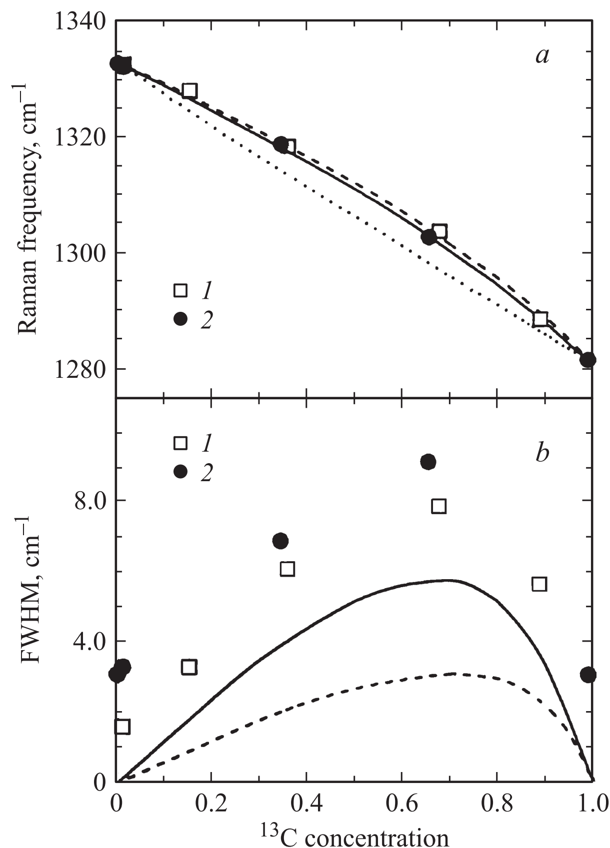

Fig. 6. Isotopic composition dependence of the (*a*) diamond Raman frequency and (*b*) linewidth (FWHM). CPA results for pure and adjusted „TPZ" models and VCA results are shown as dashed, solid and dotted lines respectively. Symbols *1* are courtesy of Chrenko et al. [30]; symbols *2* are courtesy of Hass et al. [29].

It is interesting to note that the success in describing optical phonon frequencies and Raman linewidths of isotopically mixed diamonds has not provided insights into the very strong dependence of the thermal conductivity (which depends on acoustic phonons) on small levels of isotopic disorder.

3.2. Isotope superlattices

The discussion of phonons, their dispersion and the dependence of their properties on the isotopic composition of the host crystal has so far been restricted to bulk crystals, crystals sufficiently large so as not to affect properties. What do we expect when the dimensions of the crystal are significantly reduced? The discussion in this section focuses on the fascinating features displayed by short period *isotope superlattices* consisting of alternating layers each made up of a few atomic planes of ^{A}Ge and ^{B}Ge. These are ideal structures for phonon studies because the electronic band structure is not significantly affected by the isotope superlattice, i. e., the material looks bulk-like for electrons thoughout the crystal layers.

The first problem to be addressed relates to the normal phonon of a short period isotope superlattice. The vibra-

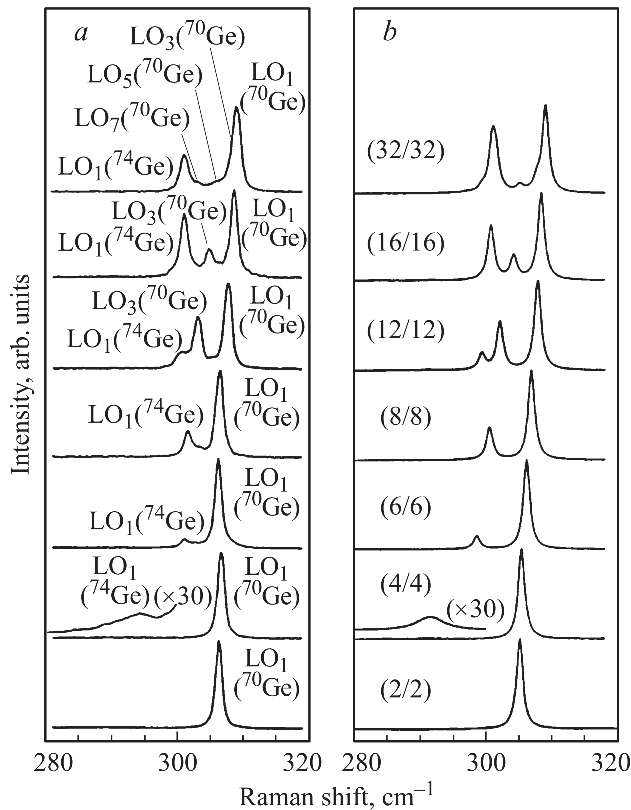

Fig. 7. a — measured at $T = 10$ K and b — calculated Raman spectra for a series of isotope superlattices $^{70}Ge_n/^{74}Ge_n$ grown along [001] with number of monolayers $n = 2$, 4, 6, 8, 12, 16, and 32. A number of modes confined to the ^{70}Ge and ^{74}Ge layers are evident (Courtesy of Spitzer et al. [32]).

tional modes and the phonon dispersion relation for a $^{70}Ge_4/^{76}Ge_4[001]$ superlattice at $\mathbf{k} = 0$ were calculated using the planar force constant model [31]. These theoretical results were tested with Raman studies of a series of MBE grown, short period isotope superlattices of ^{70}Ge and ^{74}Ge [32]. The experimental and theoretical results are summarized in Fig. 7. The shortest periods studied consisted of two atomic layers each and produce a single Raman line corresponding to the Brillouin zone center optical phonon in a Ge crystal with isotope mass $A = 72$, the arithmetic average of the two masses. Abstreiter et al., who grew this superlattice, are quite certain that this result is not due to intermixing of more than one atomic layer during growth because they used very low growth temperatures ($T = 350°$C) and low growth rates (4 Å/min). The $n = 4$ superlattice shows the Raman line predicted at $\sim 290\,\mathrm{cm}^{-1}$ though at a slightly lower intensity. In the $n = 12$ superlattice one observes at least three strong Raman lines. For $n = 32$ the Raman spectra begin to appoach the structure one would expect for two isotopically pure bulk crystals, one made up of ^{70}Ge, the other of ^{74}Ge.

Nakajima et al. [33] used Ge isotope superlattices for dynamic pump-and-probe photon studies. They recorded the oscillatory reflectivity generated by high-order coherent confined phonons (Fig. 8). While these oscillations monotonically decay in natural Ge, the isotope superlattices show a beating in the oscillation amplitude. Fourier transformation of the reflection oscillations shows directly the frequencies of the longitudinal optical (LO) phonons confined to

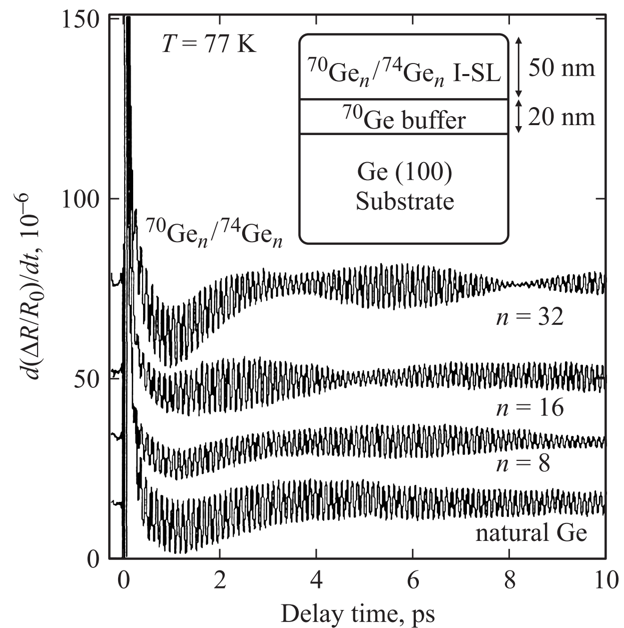

Fig. 8. Oscillatory component of the time-domain signals in $^{70}Ge_n/^{74}Ge_n$ isotope superlattices with various layer thicknesses and in natural Ge. Inset shows the structure of $^{70}Ge_n/^{74}Ge_n$ isotope superlattices (the number of monolayers $n = 8$, 16 and 32) (Courtesy Nakajima et al. [33]).

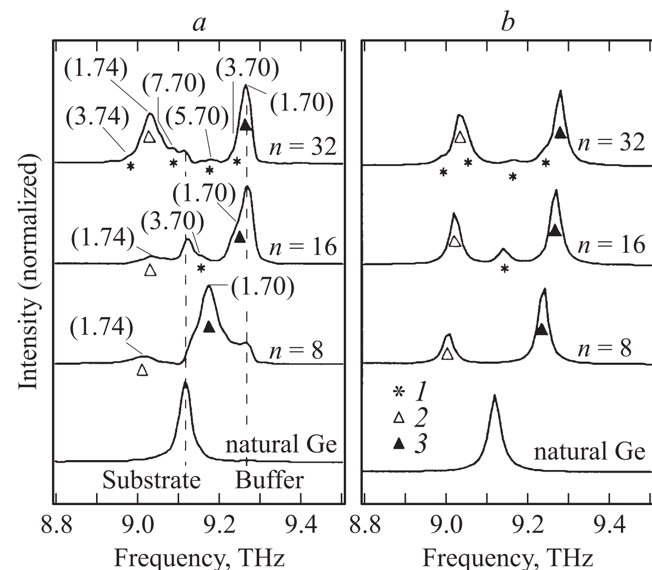

Fig. 9. a — Fourier transformed spectra of the time-domain signals shown in Fig. 10, and b — calculated spectra. (m, 70) and (m, 74) means m-th order confined modes in ^{70}Ge or ^{74}Ge layers, respectively. Vertical dashed lines in (a) denote LO phonon frequencies in the bulk ^{70}Ge buffer layers and in the natural Ge substrate. Symbols $1-3$ denote confined LO phonon modes (Courtesy Nakajima et al. [33]).

the ^{70}Ge and ^{74}Ge layers (Fig. 9). The experimental findings are in good agreement with calculations based on a planar force constant model and a bound polarizability approach [34,35].

The first silicon isotope superlattices consisting of 8, 12 and 24 atomic layers of ^{28}Si and ^{30}Si, grown and studied by Kojima et al. [36], reveal Raman spectra associated with the various confined optical phonon modes and are well reproduced theoretically by the same model used for the germanium isotope superlattices.

These Raman spectroscopy studies of Ge and Si isotope superlattices demonstrate Brillouin zone folding in a direct way. The relative intensities of the Raman lines reflect the densities of states at $\mathbf{k} = 0$. It is quite impressive how well the experimental data are reproduced by the planar bond-charge and bond polarizability models. For layers thicker than approximately 30 atomic planes we observe close to perfect localization in the individual layers, i.e., bulk-like behavior.

4. Thermal neutron absorption and transmission doping

Among the many reactions each stable isotope can undergo, we focus here on the absorption of thermal neutrons by semiconductor-forming isotopes. The major reason for this is the formation of dopant atoms as a consequence of thermal neutron capture, commonly called neutron transmutation doping (NTD).

The NTD process is typically performed in a nuclear reactor. During exposure of natural silicon to thermal neutrons all these isotopes capture neutrons with well-known capture cross sections, σ_n, and the following reactions occur:

$$^{28}_{14}\mathrm{Si} + n_{\mathrm{th}} \rightarrow {}^{29}_{14}\mathrm{Si}\ (\text{stable}), \qquad (10)$$

$$^{29}_{14}\mathrm{Si} + n_{\mathrm{th}} \rightarrow {}^{30}_{14}\mathrm{Si}\ (\text{stable}), \qquad (11)$$

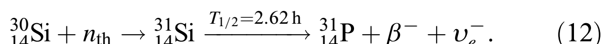

$$^{30}_{14}\mathrm{Si} + n_{\mathrm{th}} \rightarrow {}^{31}_{14}\mathrm{Si} \xrightarrow{T_{1/2}=2.62\,\mathrm{h}} {}^{31}_{14}\mathrm{P} + \beta^- + \upsilon_e^-. \qquad (12)$$

The third reaction leads to the formation of the donor P. The beta particle (electron) and the electronic anti-neutrino υ_e created in the radioactive decay escape. NTD differs from other technologies in that *very high doping uniformity* can be obtained. The unmatched doping uniformity achieved by NTD is based on three factors. First, the stable isotopes are truly randomly distributed in a semiconductor of natural composition. Second, the source of thermal neutrons is typically larger than the semiconductor crystal to be doped. This, in turn, leads to a large homogenous thermal neutron field guaranteeing identical exposure of all parts of the crystal. Third, the capture cross section for thermal neutrons is typically of the order of a few barns ($1\,\mathrm{barn} = 10^{-24}\,\mathrm{cm}^2$) which means that a few centimeters of material absorb the thermal neutron flux by significantly less than 1%, maintaining the nearly uniform neutron flux throughout the depth of the sample.

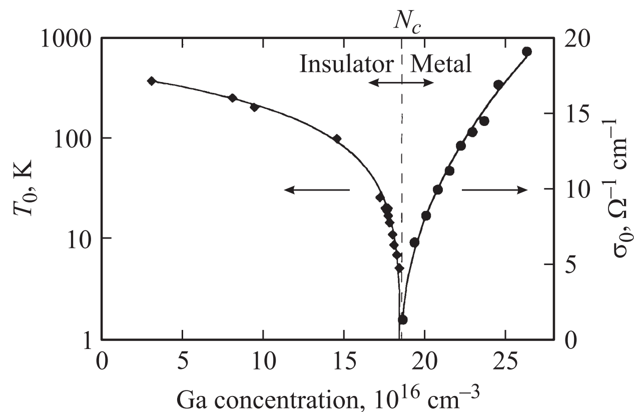

Fig. 10. Conductivity parameters for NTD ^{70}Ge below and above the metal–insulator transition. The left side shows the experimentally determined values of T_0 (Eq. (13)) of 14 insulating samples as a function of Ga concentration. The right side shows the zero temperature conductivity $\sigma(0)$ obtained from ten metallic samples as a function of Ga concentration. The critical concentrations obtained on the insulator and on the metallic side agree to within a few percent (Courtesy Itoh et al. [37]).

The combination of isotope enrichment, ultra-purification and NTD has led to p-type ^{70}Ge crystals which are homogeneously doped with a truly random Ga acceptor distribution and a donor compensation of the order 1% [37]. A series of crystals with Ga acceptor concentrations ranging from $3 \cdot 10^{16}$ to $2.6 \cdot 10^{17}\,\mathrm{cm}^{-3}$ have been studied in detail on the insulator and the metal side of the transition. Fig. 10 shows that the experimentally determined parameter T_0 as a function of the Ga concentration on the insulator side and the zero temperature conductivity $\sigma(0)$ on the metal side converge precisely at the critical concentration of $1.856 \cdot 10^{17}\,\mathrm{cm}^{-3}$. The resistivity ρ on the insulator side follows the expression developed by Shklovskii and Efros [38]:

$$\rho = \rho_0 \exp(T_0/T)^{\upsilon} \qquad (13)$$

with ρ_0 the prefactor, T_0 a constant depending on the dopant concentration and υ the critical exponent.

A significant amount of metal–insulator transition (MIT) research has been performed by the Itoh group and has been reviewed by Itoh et al. [39].

The idea of forming isotope superlattices by an epitaxial crystal growth technique and doping the various layers selectively with NTD was first proposed by this author in 1990 [40].

Isotope superlattices offer a host of new possibilities and improved processing control. The main advantage of isotope superlattices is the possibility to separate the multilayer-layer growth and the doping into two completely independent processes. The following advantages arise from this separation:

1) the growth of multilayered structures of chemically pure isotopes automatically excludes impurity auto doping,

2) layer interdiffusion is limited to host isotope self diffusion, typically one of the slowest diffusion processes in all semiconductors, and

3) using NTD, one can selectively dope the various layers after the growth process. The dopant concentration and species can be controlled by the proper selection of the isotope and its atomic concentration. The radiation damage caused by the fast neutrons accompanying the NTD process can be removed by thermal annealing at temperatures which are modest compared with the epitaxial growth temperatures.

The potential of superlattices selectively doped by NTD can be illustrated with the formation of a Ge *nipi*-structure. The necessary donors are created by neutron transmutation of ^{74}Ge into ^{75}As while the acceptors are obtained from ^{70}Ge by electron capture and ^{71}Ga formation. ^{72}Ge and ^{73}Ge can be used for the intrinsic layer or to reduce the atomic concentration of ^{70}Ge and ^{74}Ge. This may be necessary if one wants to adjust the relative doping concentrations in the *n*- and *p*-layers. Isotopic composition and doping of a hypothetical Ge *nipi*-structure may look like this:

$$[^{74}\mathrm{Ge}_x : \mathrm{As}/^{72\text{ or }73}\mathrm{Ge}_{1-x}] : [^{72\text{ or }73}\mathrm{Ge}] :$$

$$: [^{70}\mathrm{Ge}_y : \mathrm{Ga}/^{72\text{ or }73}\mathrm{Ge}_{1-y}] : [^{72\text{ or }73}\mathrm{Ge}] : \text{etc.}$$

The dopant concentrations after NTD are:

$$[\mathrm{As}] = n_{\mathrm{therm}}\sigma_{^{74}\mathrm{Ge}}xt[^{74}\mathrm{Ge}], \qquad (14)$$

$$[\mathrm{Ga}] = n_{\mathrm{therm}}\sigma_{^{70}\mathrm{Ge}}yt[^{70}\mathrm{Ge}]. \qquad (15)$$

Choosing the ratio of x and y to be the inverse of the ratio of the thermal neutron cross sections $\sigma_{^{74}\mathrm{Ge}}$ and $\sigma_{^{70}\mathrm{Ge}}$, respectively, leads to identical concentrations of As and Ga for any neutron exposure time t.

5. Diffusion

The study of self- and dopant diffusion in semiconductors has been advanced significantly through the use of isotopically controlled multilayer structures. Diffusion measurements performed with radiotracer methods are limited by the half-lives of radioactive isotopes, by the damage produced during their introduction and by near surface effects.

In contrast, the use of Secondary Ion Mass Spectrometry (SIMS) in isotope superlattice structures provides quantitative concentration profiles of the masses of the matrix as well as dopant atoms. In the simplest case, two layers with different isotopes of a semiconductor are grown on a substrate of natural composition. The results of annealing such a structure are illustrated in Fig. 11 for a $^{\mathrm{nat}}$Ge/^{74}Ge/^{70}Ge/$^{\mathrm{nat}}$Ge-substrate configuration [41]. The ^{70}Ge concentration profile in the ^{74}Ge layer can be fitted with a simple complementary error function (the solution to the 1D simple Fick's law diffusion equation) over a range of four and one half orders of magnitude in concentration, yielding very precise self-diffusion data. Similar structures of silicon isotopes have been used to obtain precise measurements of the Si self-diffusion coefficient [42].

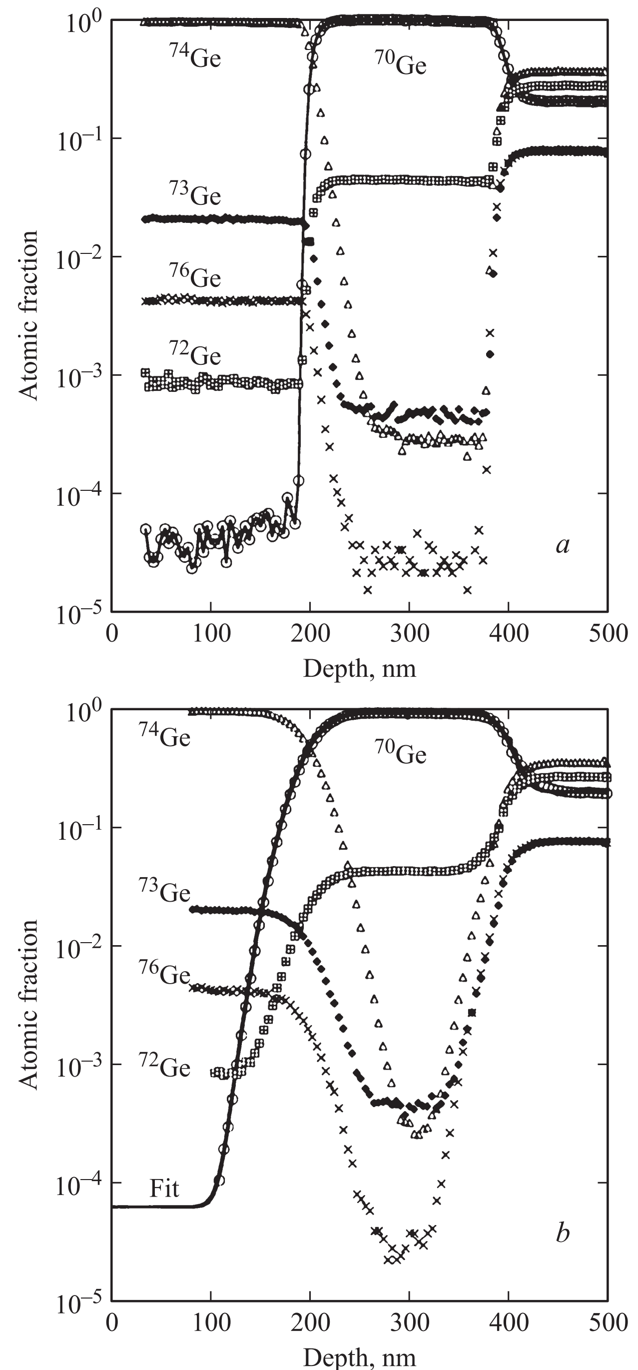

Fig. 11. Secondary ion mass spectrometry profile of a $^{\mathrm{nat}}$Ge/^{74}Ge/^{70}Ge/$^{\mathrm{nat}}$Ge-substrate structure before (*a*) and after annealing for 55.55 h at a temperature of 586°C (*b*). The self-diffusion of the ^{70}Ge into the ^{74}Ge layer can be modeled with a simple complimentary error function to a very high level of precision (Adapted with permission from Fuchs et al. [41]).

The influence of the Fermi level (and hence of specific native defects) on self- and dopant diffusion has been studied with the aid of silicon isotope multilayers capped with an amorphous layer of natural silicon. Ion-implantation into the amorphous layer was used as a source of the

desired dopant and to affect Fermi level control inside the structure. Such a dopant source has been found to produce only the expected electronic effects that are due to dopant-related shifts in Fermi level position. A representative SIMS result of silicon self- and As dopant diffusion is shown in Fig. 12. The modeling of the silicon isotope and the arsenic concentration profiles yields the unambiguous result that the negatively charged interstitial is the major native defect involved in the diffusion process [43].

Isotopically controlled compound semiconductor structures offer the possibility of observing self-diffusion of each of the constituent atoms. Using this method, a very spectacular result of self-diffusion has been reported for the III-V semiconductor GaSb. Both host elements, Ga and Sb, have two stable isotopes occuring at comparable concentrations; a double-labeled ^{69}Ga^{121}Sb/^{71}Ga^{123}Sb heterostructure was used for the study [44]. Fig. 13 shows the concentration profiles of the four isotopes ^{69}Ga, ^{71}Ga, ^{121}Sb and ^{123}Sb for the as-grown structure and after thermal annealing at different times and temperatures. The Ga host atoms diffuse by a factor of ~ 1000 faster than the Sb atoms. Even after 4 days at a temperature just under the bulk melting point of GaSb and long after the labeled Ga atoms have diffused into the bulk, the Sb atoms have barely moved. The large difference can be explained with the formation of Ga_{Sb} antisites that suppress the formation of Sb vacancies required for the diffusion of this constituent. An in-depth discussion of diffusion in a number of isotopically controlled semiconductors is given in an article by Bracht, Silvestri and Haller [45].

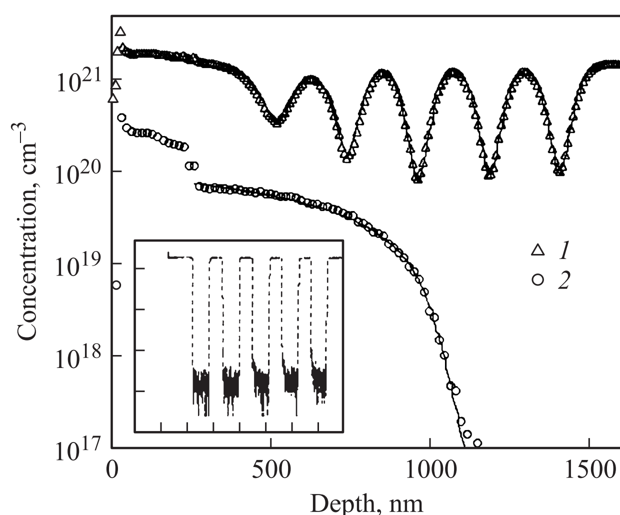

Fig. 12. Depth profiles of ^{30}Si (*1*) and As (*2*) in an *a*-Si/(^{30}Si/^{nat}Si)/^{nat}Si structure with 5 ^{30}Si/^{nat}Si periods, measured with secondary ion mass spectrometry. Consistent modeling of both the dopant, As, and self-diffusion profiles (solid lines) shows that the singly negatively charged self-interstitial is the mediating native defect responsible for the diffusion of both species. Inset figure shows the SIMS depth profile of the as-grown isotope structure, with the same axis limits (Adapted with permission from H.H. Silvestri, Ph.D. Thesis, UC Berkeley (2004), unpublished [43]).

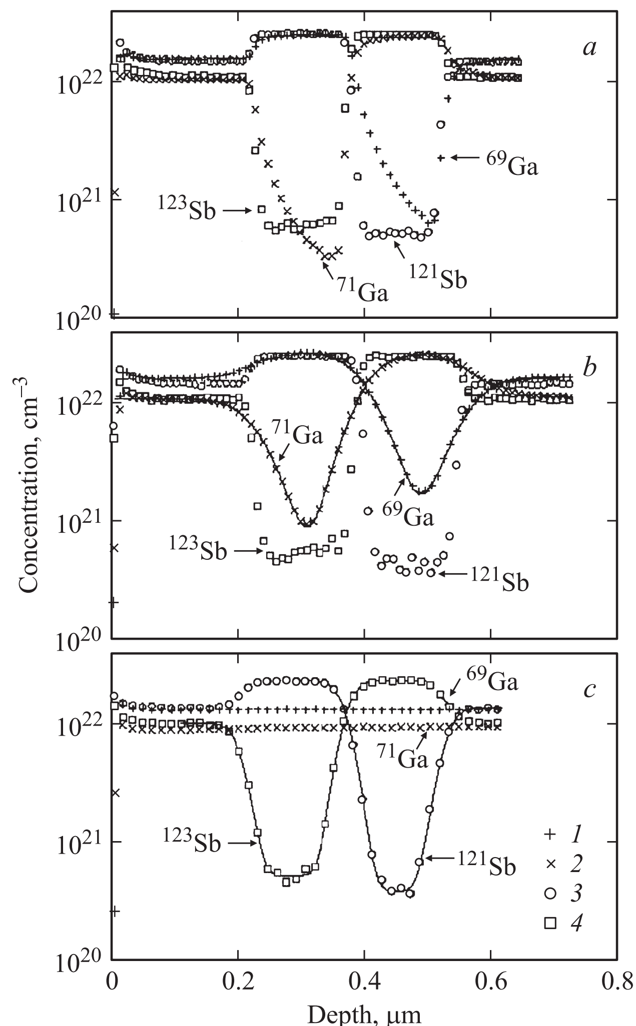

Fig. 13. Concentration-depth profiles of Ga and Sb isotopes in GaSb isotope heterostructures measured with SIMS. Data are shown for ^{69}Ga (*1*), ^{71}Ga (*2*), ^{121}Sb (*3*) and ^{123}Sb (*4*). *a* — Ga and Sb profiles of the as-grown ^{69}Ga^{121}Sb/^{71}Ga^{123}Sb heterostructure. *b, c* — profiles after annealing the isotope structure under Sb-rich conditions at 700°C for 105 min (*b*) and 18 days (*c*). The Ga and Sb diffusion coefficients were determined by fitting the solution of Fick's law for self-diffusion across an interface to the Ga and Sb profiles measured after annealing. Solid lines in *b* and *c* show best fits (Adapted with permission from Bracht, et al. [44]).

6. Local vibrational mode spectroscopy

Local vibrational mode (LVM) spectroscopy is a well-established tool for the study of defects and low mass impurities in semiconductors [46,47]. Isotope substitution has been widely used to identify the particular impurity producing a given LVM signature. Perhaps the most widely used isotope substitution is that of *H* by *D*. With the vibrational frequency depending on the inverse square root of the isotope mass, the shift in frequency from a *H*- to a *D*-related LVM is close to 40%.

A less pronounced effect is the dependence of an LVM spectrum on the mass of the neighboring host atoms. To the

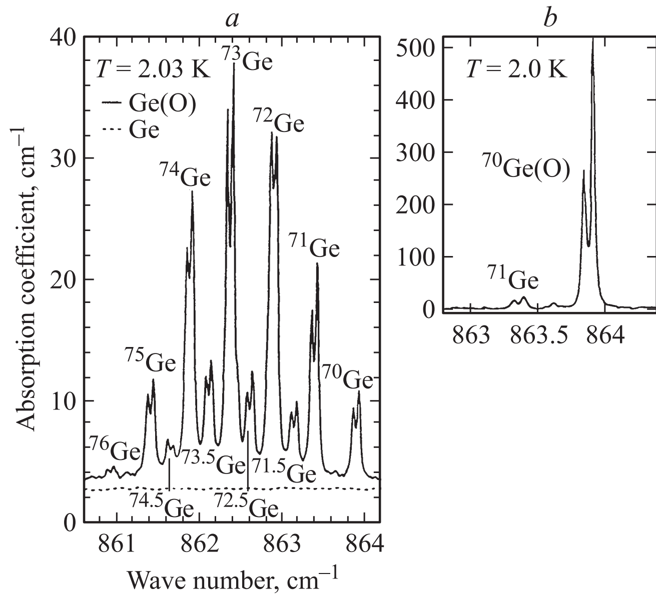

Fig. 14. a — spectrum of the Ge_2O quasi molecules in natural Ge at 2.05 K. Eleven lines split bu $\upsilon_2 + \upsilon_3$ coupling excitations correspond to the distinct isotopic mass combinations of the two Ge atoms in the quasi molecule. An oxygen sample free sample produced the dashed line. b — the spectrum of an oxygen doped, highly enriched sample of ^{70}Ge. The lines labled ^{71}Ge are caused by traces of ^{72}Ge in ^{70}Ge (Courtesy Mayur et al. [50]).

extent the mass of neighboring atoms is not infinite, it is of interest to explore to what extent they participate in the vibrational motion of the impurity. Isotope control of the semiconductor host lattice offers a direct identification of the various atoms participating in the local vibration.

As an illustrative example of a LVM frequency being affected by the host atoms, we briefly review the LVM structure of O in natural and isotopically controlled Ge [14]. To model the LVM of this bond centered impurity, one takes into account the two nearest neighbors, while the rest of the lattice appears as a small correction, called „interaction mass“. The ^{x}Ge-O-^{y}Ge molecule has three fundamental modes. The „wag“ mode (υ_3) has the highest frequency and was observed in oxygen rich Ge quite some time ago [48]. Low-temperature, high resolution studies show eleven lines, each one split into several components whose intensities depend on temperature [49]. The eleven lines result from the different mass combinations of ^{x}Ge and ^{y}Ge. Combinations with identical linear mass averages (e. g. ^{72}Ge/^{74}Ge and ^{73}Ge/^{73}Ge) lead almost to the same oxygen vibrational frequencies.

The complexity of such spectra can be reduced very significantly through the use of isotopically pure (or at least highly enriched) crystals. Fig. 14 shows two spectra which were reported by Mayur et al. [50]. They used one natural and four highly enriched Ge crystals doped with oxygen. The reduction from eleven to one LVM line is significant because it allows a quantitative study of the linewidth and of the coupling between υ_3 and the other modes as a function of temperature. The splitting is a result of the nonlinear superposition of the υ_2 and the υ_3 modes. The low frequency υ_2 modes can be thermally populated already near liquid helium temperature.

7. Optical spectroscopy of shallow dopants and deep level centers

7.1. Shallow dopant absorption spectroscopy

Shallow acceptors and donors in semiconductors can be described to first order with the hydrogenic model, i. e., the energy of the ground and bound excited states is given by the equation for the hydrogen atom modified by replacing the electron mass with the effective mass and multiplying the permitivity of vacuum, ε_0, with the dielectric constant of the semiconductor, ε.

$$E_{\mathrm{D,A}} = \frac{e^4 m_e}{2(4\pi\varepsilon_0 h)^2}\,\frac{m^*}{m_e}\,\frac{1}{\varepsilon^2}. \tag{16}$$

These modifications lead to very small ground state energies, in the tens of meV, which is optically in the far infrared region of the electromagnetic spectrum. The Bohr radii, on the other hand, are very large, of the order of tens to over 100 Å. The ground state to bound excited state transitions have been recorded with absorption spectroscopy for many shallow donors and acceptors in numerous semiconductors. An excellent review of donors and acceptors in silicon and germanium has been published by A.K. Ramdas and S. Rodriguez [51]. In order to obtain high resolution spectra, one has to study high purity crystals of excellent crystalline quality. With a net-dopant concentration of $< 10^{10}\,\mathrm{cm}^{-3}$, ultra-pure germanium which is used for the fabrication of large volume gamma ray detectors, is the purest, structurally most perfect semiconductor. The absorption strength of the residual acceptors and donors is too small to obtain far IR spectra.

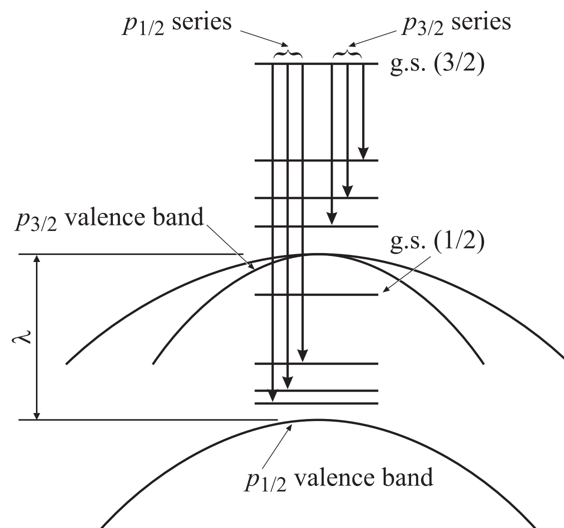

Fig. 15. Energy diagram for shallow acceptors in silicon (Courtesy Onton et al. [54]).

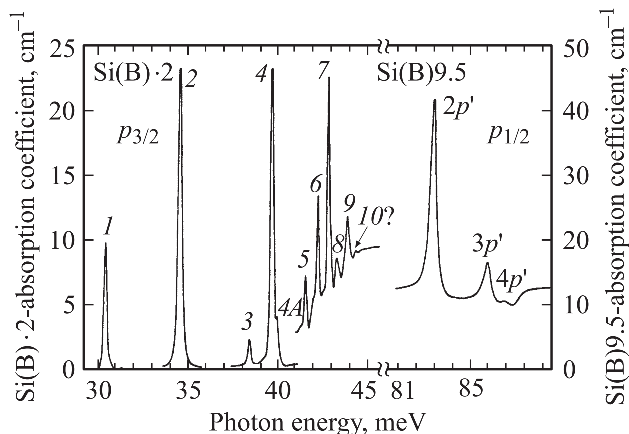

Fig. 16. The excitation spectrum of boron in silicon recorded at 4.2 K (Courtesy Onton et al. [54]).

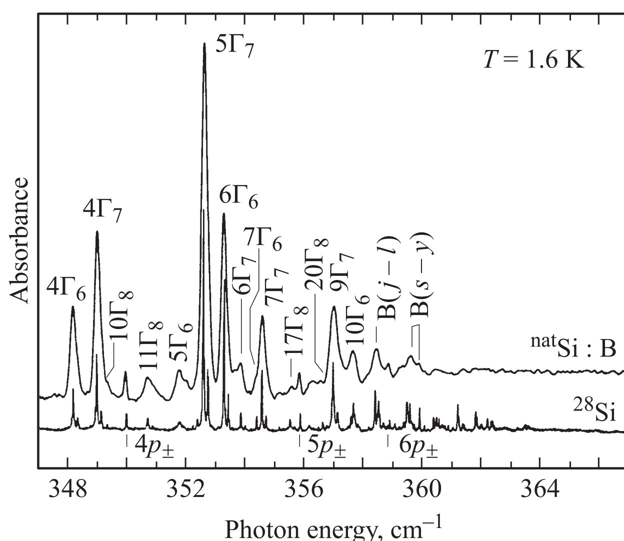

Fig. 17. The energy resolution of the boron acceptor spectrum in ^{nat}Si increases dramatically when boron in highly enriched ^{28}Si is studied. Each boron related absorption line is split into two components with a line strenth ratio corresponding to the ratio of the ^{10}B and ^{11}B isotope abundance. This tells us that the boron ground state is sensitive to the boron nuclear mass (Courtesy Steger et al. [55]).

Photo Thermal Ionization Spectroscopy (PTIS), based on a discovery by T.M. Lifshitz and Ya. Nad [52] overcomes this problem and has delivered very high resolution spectra [53]. Can the resolution be increased with isotopically enriched semiconductors? The answer is affirmative for shallow acceptors and donors in silicon. Fig. 15 shows the top of the valence band for silicon. The top is degenerate for light and heavy $p_{3/2}$ holes and there exists a split-off $p_{1/2}$ hole band (spin-orbit splitting). Transitions can occur between the ground state and the bound excited states of both bands, producing two series of lines as shown in Fig. 16. For high resolution spectroscopy the samples must be cooled to liquid He temperature.

The energy region between 43 and 45 meV is shown expanded in Fig. 17 for ^{nat}Si and for highly enriched ^{28}Si.

7.2. Photoluminescence

Photoluminescence (PL) is an optical technique which complements absorption spectroscopy in several ways. A piece of semiconductor, cooled to liquid He temperature, is illuminated with near or above bandedge light. Absorption of such photons leads to free electrons and holes. Electrons and holes can bind through Coulomb forces, forming excitons. In an indirect bandgap semiconductor free excitons can only decay with the emission or absorption of a phonon which provides the crystal momentum conservation. Free excitons moving through the crystal, in turn, can get bound to dopants or defects. In this case no phonons are required for momentum conservation. An exciton bound to a neutral acceptor consists of the negatively charged acceptor core, two holes and one electron, quite a complicated structure! Electron-hole recombination of bound excitons produced rich spectra, characteristic for the center to which the exciton was bound. Fig. 18 shows PL emission spectra of boron doped ^{nat}Si and ^{28}Si. Again, the reduction in linewidth due to the enrichment is impressive. Indeed, the PL spectral resolution of ^{28}Si is limited by the spectrometer. When the *absorption spectrum* of the same crystal is recorded with an extremely narrow tunable laser line, a much sharper PLE (excitation PL) spectrum is created (bottom spectrum).

PL spectra of donor bound excitons also experience vast resolution improvements when enriched ^{28}Si crystals are studied. Fig. 19 displays the PL spectra of excitons bound to P donors in both ^{nat}Si and ^{28}Si. A small magnetic field of 490 G leads to a Zeemann splitting of the lines.

Excitons bind not only to shallow dopants but to deep centers as well. Deep center PL with isotopically enriched ^{28}Si has led to quite unexpected results which are making earlier assignments of impurities to specific

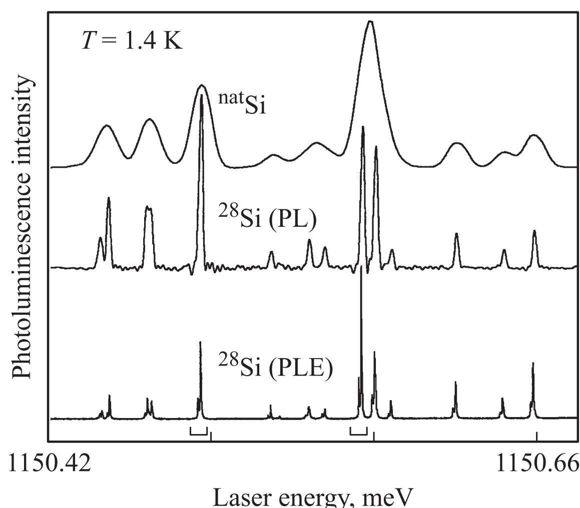

Fig. 18. Photoluminescence and photoluminescence excitation spectra of B doped ^{nat}Si and ^{28}Si (Courtesy Thewalt et al. [56]).

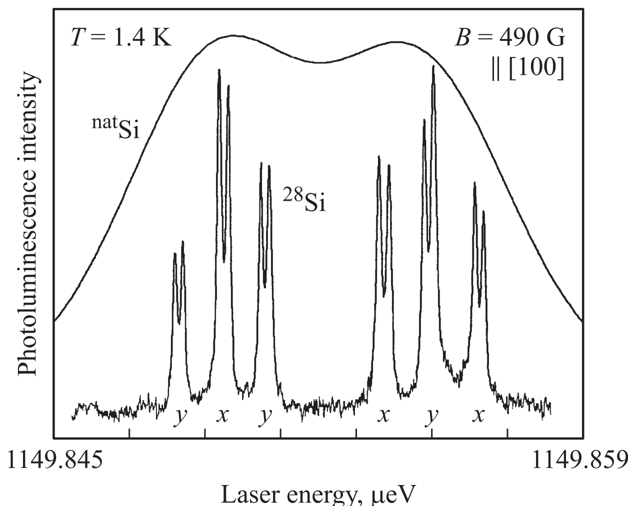

Fig. 19. The photoluminescence excitation Zeeman spectrum of the ^{31}P bound exciton no-phonon transitions in a highly enriched ^{28}Si sample with a small applied magnetic field. The doublets labeled x and y arise from hyperfine splitting of the donor ground state (Courtesy Thewalt et al. [57]).

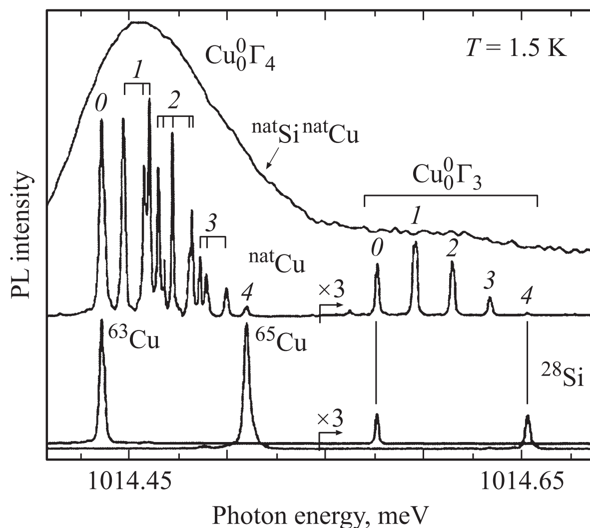

Fig. 20. The Cu$^0_0$ no-phonon lines ($\sim$ 1014 meV) in ^{nat}Si diffused with ^{nat}Cu (top, down-shifted by 62 μeV for clarity) are compared with those in ^{28}Si samples diffused with either ^{nat}Cu (middle) or enriched ^{63}Cu or ^{65}Cu (bottom). $N = 0, \ldots, 4$ denotes the number of ^{65}Cu in the Cu$_4$ complex. Γ_4 is the ground state transition and Γ_3 is a low lying electronic excited state (Courtesy M. Steger et al. [58]).

deep centers questionable. It is again the group of Thewalt working with enriched silicon that has made major contributions. As an example, the copper related center which generates a no-phonon line at 1014 meV has been assigned to a copper pair. There is theoretical support for this assignment. Figure 20 shows this broad NP spectrum for natural Si diffused with natural Cu [58]. Using ^{28}Si and only one of the two Cu isotopes, either ^{63}Cu or ^{65}Cu, reduces this spectrum to two sharp lines seen at the bottom of Fig. 20. Introducing both Cu isotopes into enriched ^{28}Si creates the very rich spectrum shown in the middle of Fig. 20. This spectrum can be uniquely assigned to a Cu$_4$ complex. The Thewalt group has investigated several deep level centers in enriched ^{28}Si and they find that in the most extreme cases the impurity to which a center was assigned is not at all present! It looks like there are a number of surprises in store, especially if this approach also works for other semiconductors.

8. Nuclear spin

A number of elements found in typical semiconductors have half-odd nuclear spins I and hence magnetic moments. Examples are ^{73}Ge ($I = 9/2$), ^{29}Si ($I = 1/2$), ^{31}P ($I = 1/2$), and both stable isotopes of Ga: ^{69}Ga ($I = 1/2$) and ^{71}Ga ($I = 1/2$). The magnitude of the magnetic moment and the spin-lattice (T_1) and transverse (decoherence, T_2) lifetimes of non-equilibrium nuclear spin populations are measured with nuclear magnetic resonance (NMR). In high-quality single crystal material, lifetimes can be long. For example, the spin lattice relaxation time of the ^{29}Si (4.67% natural abundance) nuclear spin can be as long as several hours at room temperature in high purity single crystals; decoherence times are on the order of milliseconds at cryogenic temperatures. In the case of electron spin resonance (ESR), soon after the demonstration of the effect in the late 1950's, the effects of isotopic enrichment on the spin dynamics of donor electrons bound to ^{31}P were investigated. At that time, a doubling of T_2 from 0.2 to 0.5 ms was observed by removing the hyperfine spin orbit coupling interaction between the electron spin and the nuclear spin of the ^{29}Si. Modern measurements on more than 99% enriched, higher purity 99% ^{28}Si have demonstrated $T_2 > 60$ ms. These and related effects are expected to be important in the solid state quantum computing shemes based on electron and/or nuclear spin as „qu-bits" [59–62]. An in-depth account of the state of quantum computing with isotopically controlled semiconductor structures will be given in the accompanying paper by K.M. Itoh.

9. Conclusions and outlook

An impressive amount of research with isotopically controlled semiconductors has accumulated over the past 20 years. The major effects due to the different isotope nuclear masses have been measured in many semiconductors and they are theoretically understood. The exploitation of spin properties has only started and the prospects for a silicon based quantum computer making use of either the nuclear spin of ^{29}Si or the spin of an electron bound to a phosphorus donor is fascinating. Sizable quantities of isotopically enriched high quality crystalline silicon have only become available recently and have led to record resolution

photoluminescence and infrared absorption spectroscopy of dopants [71,72]. Many more interesting results with isotopically enriched bulk and thin film semiconductor structures can be expected, especially for alloy and compound materials, magnetic semiconductors and nano-structured materials systems. Solid state diffusion will continue to profit from isotope tracers and neutron transmutation doping may be used for further metal–insulator transition investigations (As doped ^{74}Ge is an obvious choice!) and for doping of nanocrystals. The study of neutron transmutation doping of enriched ^{30}Si is of particular interest because only 1/30 of the neutron exposure leads to the same phosphorus concentration obtained in natural Si! The 30 times smaller fast neutron damage should result in much higher quality material with larger minority carrier lifetime.

I have enjoyed many fruitful collaborations working with a large number of individuals and groups with isotopically enriched semiconductors. I owe all of them a great deal and I would like to express my sincere gratitude to each one. Much of this research became possible because of the courage of Valerii Ozhogin of the Kurchatov Institute who made the first sizable quantities of enriched ^{70}Ge and ^{74}Ge available for scientific collaborations.

Some of the reviewed work has been supported in part by the Director, Office of Science, Office of Basic Energy Sciences, Division of Materials Science and Engineering, of the U.S. Department of Energy under contract No. DE-AC02-05CH11231, and in part by U.S. NSF Grants No. DMR-0109844 and DMR-0405472.

References

[1] F. Soddy. Ann. Rep. Prog. Chem., VII, 256 (1910); Nature, **91**, 57 (1913).
[2] J.J. Thomson. Proc. Royal Soc. A, **89**, 1 (1913).
[3] F.W. Aston. *Mass Spectra and Isotopes* (Edward Arnold, London, 1942) p. 4.
[4] T.H. Geballe, G. Hull. Science, **250**, 1194 (1958).
[5] M. Cardona, private communication.
[6] J.M. Ziman. *Electrons and Phonons* (Oxford University Press, London, 1963) p. 288.
[7] D.T. Morelli et al. In: *Proc. 2nd Int. Conf. on New Diamond Science and Technology* (MRS, Pittsburgh, 1991) p. 869.
[8] I. Pomeranchuk. J. Phys. (Moscow), **6**, 237 (1942).
[9] L. Wei et al. Phys. Rev. Lett., **70**, 3764 (1993).
[10] J. Callaway. Phys. Rev., **113**, 1046 (1959).
[11] T.H. Geballe. Science, **250**, 1194 (1990).
[12] J.R. Olson et al. Phys. Rev. B, **47**, 14 850 (1993).
[13] V.I. Ozhogin et al. JETP Lett., **63**, 490 (1996).
[14] V. Asen-Palmer et al. Phys. Rev. B, **56**, 9431 (1997).
[15] T. Ruf et al. Sol. St. Commun., **115**, 243 (2000); Erratum, Sol. St. Commun., **127**, 257 (2003).
[16] A.V. Inyushkin. Inorg. Mater., **38**, 427 (2002).
[17] L. Vegard. Z. Phys., **5**, 17 (1921).
[18] L. Nordheim. Ann. Phys., **9**, 607 (1931).
[19] H.D. Fuchs et al. Sol. St. Commun., **82**, 225 (1992).
[20] H.D. Fuchs et al. Phys. Rev. B, **44**, 8633 (1991).
[21] H.D. Fuchs et al. Phys. Rev. B, **43**, 4835 (1991).
[22] P. Etchegoin et al. Sol. St. Commun., **83**, 843 (1992).
[23] M. Cardona et al. J. Non-Cryst. Sol., **141**, 257 (1992).
[24] M. Cardona et al. J. Phys. Condens. Matter, **5**, A61 (1993).
[25] P.W. Anderson. Phys. Rev., **109**, 1492 (1955).
[26] G. Davies et al. Semicond. Sci. Technol., **7**, 1271 (1992).
[27] G. Davies et al. Semicond. Sci. Technol., **8**, 127 (1993).
[28] K.C. Hass et al. Phys. Rev. B, **44**, 12 046 (1991).
[29] K.C. Hass et al. Phys. Rev. B, **45**, 7171 (1992).
[30] R.M. Chrenko et al. J. Appl. Phys., **63**, 5873 (1988).
[31] H.D. Fuchs et al. Superlatt. Microstruct., **13**, 447 (1993).
[32] J. Spitzer et al. Phys. Rev. Lett., **72**, 1565 (1994).
[33] M. Nakajima et al. Phys. Rev. B, **63**, 161 304 (R) (2001).
[34] B. Jusserand, M. Cardona. In: *Light Scattering in Solids V*, eds M. Cardona and G. Güntherodt (Springer-Verlag, Berlin, 1989) p. 49.
[35] P. Molinàs-Mata, M. Cardona. Phys. Rev. B, **43**, 9799 (1991).
[36] T. Kojima et al. Appl. Phys. Lett., **83**, 2318 (2003).
[37] K.M. Itoh et al. Phys. Rev. Lett., **77**, 4058 (1996).
[38] B.I. Shklovskii, A.L. Efros. *Electronic Properties of Doped Semiconductors, Solid State Series*, Vol. 45 (Springer-Verlag, Berlin, 1984).
[39] K.M. Itoh et al. J. Phys. Soc. Jpn., **73**, 173 (2004).
[40] E.E. Haller. Semicond. Sci. Technol., **5**, 319 (1990).
[41] H. Fuchs et al. Phys. Rev. B, **51**, 16 817 (1995).
[42] H. Bracht et al. Phys. Rev. Lett., **81**, 393 (1998).
[43] H.H. Silvestri, Ph.D. Thesis. UC Berkeley, 2004, unpublished.
[44] H. Bracht et al. Nature, **408**, 69 (2000).
[45] H.A. Bracht et al. Sol. St. Commun., **133**, 727 (2005).
[46] A.S. Barker, A.J. Sievers. Rev. Mod. Phys., **47**, Suppl. 2 (1975).
[47] E.E. Haller. Mater. Res. Soc. Symp. Proc., **378**, 547 (1995).
[48] W. Kaiser et al. Phys. Rev., **101**, 1264 (1956).
[49] B. Pajot, P. Clauws. In: *Proc. 18th Int. Conf. on the Physics of Semiconductors*, ed. O. Engström (Word Scientific, Singapore, 1987) p. 911.
[50] A.J. Mayur et al. Phys. Rev. B, **49**, 16 293 (1994).
[51] A.K. Ramdas, S. Rodriquez. Rep. Progr. Phys., **44**, 1297 (1981).
[52] T.M. Lifshits, F.Y. Nad. Doklady Akademii Nauk SSSR, **162**, 801 (1965).
[53] E.E. Haller et al. IEEE Trans. Nucl. Sci. **NS-22**, No 1, 127 (1975).
[54] A. Onton et al. Phys. Rev., **163**, 686 (1967).
[55] M. Steger et al. Phys. Rev. B, **79**, 2 052 190 (2009).
[56] M.L.W. Thewalt et al. J. Appl. Phys., **101**, 081 724 (2007).
[57] A. Yang et al. Phys. Rev. Lett., **97**, 227 401 (2006).
[58] M.Steger et al. Phys. Rev. Lett., **100**, 177 402 (2008).
[59] B.E. Kane. Fortschritte der Physik-Progress of Physics, **48**, 1023 (2000).
[60] K.M. Itoh, E.E. Haller. Physica E, **10**, 463 (2001).
[61] T.D. Ladd et al. Phys. Rev. Lett., **89**, 011 901 (2002).
[62] John J.L. Morton et al. Nature, **455**, 1085 (2008).

Редактор Т.А. Полянская